LARGE EDDY SIMULATION OF AN ADVANCING ROTOR FOR THE CHARACTERIZATION OF WAKE SIGNATURE AND WAKE ENCOUNTER SEVERITY ON FINAL APPROACH

G. Querinjean*, V. Colognesi*†, M. Duponcheel*, G. Poncelet*, D.-G. Caprace*, P. Chatelain*, G. Winckelmans*

*Institute of Mechanics, Materials and Civil Engineering, UCLouvain, 1348 Louvain-la-Neuve, Belgium
†Department of Biology, Lund University, Lund, Sweden

Abstract

In this work, Large Eddy Simulations of the wake shed by a helicopter rotor in forward flight are performed using a hybrid Eulerian-Lagrangian Vortex Particle-Mesh (VPM) method. Fundamental wake properties are measured. The influence of the flight speed on the wake is investigated, from a high speed of 100 kt to a very low speed of 12.5 kt. At high airspeed, the wake rolls up in a typical compact two-vortex system. The vortex circulation is thus inversely proportional to the flight speed. At low airspeed, the wake departs from this simple behavior. The vortex spacing increases and the wake becomes overwhelmed by turbulence. The circulation is then no longer directly related to the flight speed. The VPM method is also used to measure the aerodynamic loads felt by a rotorcraft when crossing a wake. The main perturbation is found to be a pitching moment. The results show a proportionality relationship between the latter and the airspeed of the follower rotorcraft.

1. NOTATION

b	Aircraft wing span	m	U_∞	Flight speed	$\mathrm{m\,s^{-1}}$
b_0	Wake vortices spacing	m	$\boldsymbol{x}_p$	Particle position	m
D	Main rotor diameter	m	y	Lateral coordinate	m
L	Lift force	N	z	Vertical coordinate	m
$L_{x/y/z}$	Dimensions of the CFD domain	m	$\boldsymbol{\alpha}_p$	Vortex particle strength	$\mathrm{m^3\,s^{-1}}$
M_{Roll}	Rolling moment	N m	β	Blade flap angle	deg
M_{Ritch}	Pitching moment	N m	γ	Glide slope	deg
M_{Yaw}	Yawing moment	N m	$\Gamma(r)$	Vortex circulation distribution	$\mathrm{m^2\,s^{-1}}$
r	Distance to a vortex center	m	Γ_0	Total vortex circulation	$\mathrm{m^2\,s^{-1}}$
r_c	Vortex core radius	m	$\tilde{\Gamma}_0$	Half-plane circulation	$\mathrm{m^2\,s^{-1}}$
t	Wake age	s	ϵ	Eddy dissipation rate	$\mathrm{m^2\,s^{-3}}$
t^*	Dimensionless wake age	-	ν	Air kinematic viscosity	$\mathrm{m^2\,s^{-1}}$
t_0	Wake vortex characteristic time	s	θ	Blade pitch angle	deg
$\boldsymbol{u}$	Velocity field	$\mathrm{m\,s^{-1}}$	θ_0	Collective pitch angle	deg
u_θ	Vortex induced velocity	$\mathrm{m\,s^{-1}}$	θ_{1c}	Longitudinal cyclic pitch angle	deg
$\boldsymbol{u}_\omega$	Rotational velocity field	$\mathrm{m\,s^{-1}}$	θ_{1s}	Lateral cyclic pitch angle	deg
V_0	Wake vortex characteristic velocity	$\mathrm{m\,s^{-1}}$	$\theta_{1s,eq}$	Equivalent cyclic angle	deg
w_s	Wake vortex sink rate	$\mathrm{m\,s^{-1}}$	$\theta^*_{1s,eq}$	Theoretical equivalent cyclic angle	deg
x	Streamwise coordinate	m	ρ	Air density	$\mathrm{kg\,m^{-3}}$

$\boldsymbol{\omega}$	Vorticity field	s^{-1}
Ω	Rotor angular velocity	s^{-1}
$\lVert\cdot\rVert$	Vector norm	-
$\overline{\cdot}$	Time-averaging operator	-
AC	Fixed-wing aircraft	-
CFL	Courant number	-
RC	Rotorcraft	-
RMC	Rolling moment coefficient	-
TAS	True Airspeed	$\mathrm{m\,s}^{-1}$
VPM	Vortex Particle-Mesh	-

2. INTRODUCTION

The predicted growth of air traffic in the coming decades and the rise of concerns related to the associated environmental and noise footprints will stress future ATC systems in unprecedented ways, posing operational and safety challenges to capacity-constrained airports striving to improve their runway throughput. In this regard, the optimization of safe air traffic separation policies is of prime importance.

The decisive role played by wake turbulence in aircraft separation management has driven considerable research efforts towards the characterization and categorization of aircraft wakes, entailing regulations that have enabled ever more efficient and safer airport operation. However, most of the scientific endeavor that led to widely used wake severity metrics such as RECAT-EU (Ref. 1) has been restricted to fixed-wing aircraft (Refs. 2,3,4). Rotorcraft have so far not been included in those metrics, a fact primarily attributable to the limited number of airports concerned with frequent and heavy helicopter traffic. However, the rise of urban air mobility promises a global increase in rotorcraft traffic in mixed airspaces including already busy airports, which justifies the need for appropriate separation criteria. The complexity of rotorcraft wake dynamics renders the establishment of metrics difficult. Only a handful studies have tackled this subject based on first principles (Ref. 5) or using Computational Fluid Dynamics (CFD) (Refs. 6,7). Even fewer have thoroughly characterized the far wake (Refs. 8,9). To the authors knowledge, a similar shortfall of high-fidelity CFD investigation subsists for vortex encounters involving a rotorcraft (Ref. 10). Moreover, an additional difficulty in rotorcraft wake categorization arises from the great variability of their wake signature in the context of airport operation: unlike fixed-wing aircraft, their approach speed can indeed lie anywhere between near-zero (when taxiing over the runway) and their rated airspeed, causing more potent wake vortices at lower speeds.

This work aims at providing new insights into the low-speed wake phenomena typical of the final approach and hover-taxi phases of helicopters, building upon numerical simulations of their wake, obtained using a state-of-the-art Large Eddy Simulation (LES) flow simulation framework specialized in the capture of the far wake. In the present study, the rotorcraft is considered from two standpoints: once as a leader, i.e., as a wake generator; then as a follower, encountering a wake shed by a leader rotorcraft or aircraft. The object of the paper is thus twofold.

First, a refined characterization of the rotorcraft wake signature is achieved at four airspeeds: 100, 50, 25 and 12.5 kt (1 kt = 0.5144 $\mathrm{m\,s}^{-1}$). Fundamental aerodynamic quantities are extracted from the CFD simulations and leveraged to shed light on the distinctiveness of rotorcraft wakes with respect to fixed-wing aircraft of similar size and weight in final approach phase of flight. The effect of the airspeed on the rotorcraft wake properties is investigated, and the risk posed by the wake vortices on a follower aircraft is evaluated using the simplified rolling moment coefficient (RMC) metric.

Second, the resistance of rotorcraft to wake vortex encounters is quantified. The aerodynamic forces and moments that result from the interaction of the rotor with the wake are measured, and the sensitivity of the perturbation to the flight speed of the follower rotorcraft is studied, with airspeeds of 100, 50, and 25 kt. Then, in an effort to provide a metric similar to those used for regulations applicable to fixed-wing aircraft (such as the RMC metric), a metric for rotorcraft wake encounters is assessed by comparing the perturbation predicted by the metric with that measured in the CFD simulations.

3. METHOD

The present work builds upon Large Eddy Simulations of a four-bladed rotor based on available data of the Airbus Helicopter H135 main rotor, performed using a numerical method coupling the multi-body integrator `ROBOTRAN` with a massively parallel Vortex Particle-Mesh (VPM) solver. The former is responsible for the rigid blade dynamics and rotor control inputs, and the latter for the bulk flow simulation.

3.1. Flow solver

The flow solver (Ref. 11) relies on a hybrid Eulerian-Lagrangian formulation of the incompressible ($\nabla \cdot \boldsymbol{u} = 0$) Navier-Stokes equations in their vorticity-velocity formulation ($\boldsymbol{\omega} - \boldsymbol{u}$):

$$\frac{D\boldsymbol{\omega}}{Dt} = (\nabla \boldsymbol{u}) \cdot \boldsymbol{\omega} + \nu \nabla^2 \boldsymbol{\omega} \tag{1}$$

where $\frac{D}{Dt} \triangleq \frac{\partial}{\partial t} + \boldsymbol{u} \cdot \nabla$ denotes the material derivative. The incompressible velocity field is decomposed as

$$\boldsymbol{u} = \boldsymbol{U}_\infty + \boldsymbol{u}_{\boldsymbol{\omega}} \tag{2}$$

where $\boldsymbol{U}_\infty$ is the free stream velocity (i.e., the flight speed) and $\boldsymbol{u}_{\boldsymbol{\omega}}$ is retrieved from the vorticity field through the resolution of a Poisson equation:

$$\nabla^2 \boldsymbol{u}_{\boldsymbol{\omega}} = -\nabla \times \boldsymbol{\omega} \ . \tag{3}$$

The advection term of the Navier-Stokes equations, which corresponds to the left-hand side of Eq. (1), is handled using Lagrangian vorticity-carrying particles, each characterized by a position $\boldsymbol{x}_p$ and a strength $\boldsymbol{\alpha}_p = \int_{V_p} \boldsymbol{\omega} \, d\boldsymbol{x}$, where V_p corresponds to the material volume associated to the particle. This Lagrangian treatment of the flow allows to write Eq. (1) as two sets of ODE's for the particles:

$$\frac{d\boldsymbol{x}_p}{dt} = \boldsymbol{u}\left(\boldsymbol{x}_p\right) \ , \tag{4}$$

$$\frac{d\boldsymbol{\alpha}_p}{dt} = \int_{V_p} \left[(\nabla \boldsymbol{u}) \cdot \boldsymbol{\omega} + \nu \nabla^2 \boldsymbol{\omega} \right] \, d\boldsymbol{V}_p \ . \tag{5}$$

Both ODE's are integrated in time using a third-order Runge-Kutta scheme.

The right-hand side of Eq. (5), which comprises the stretching and diffusion terms, is discretized using fourth-order finite differences on an underlying Cartesian mesh, thus conferring a Eulerian character to the solver.

The Poisson equation Eq. (3) must be solved at each timestep to retrieve the velocity field. Its numerical resolution also exploits the background Cartesian mesh as it is solved in the Fourier space using the PPM library (Ref. 12). This allows the enforcement of unbounded and inlet/outlet boundary conditions.

In Large Eddy Simulations, only a fraction of the turbulence scales are resolved. The unresolved fine scales must be taken into account through an added sub-grid scale (SGS) model, here implemented as in Ref. 13.

The hybrid particles-mesh discretization of the flow requires mesh-to-particles and particles-to-mesh interpolations, which are carried out using high-order kernel schemes. In order to alleviate the loss of accuracy due to the phenomenon of particles clustering and depletion, a periodic remeshing of the particles is performed by redistributing the vorticity carried by the particles onto the underlying mesh. As the method does not preserve the solenoidal character of the vorticity field ($\nabla \cdot \boldsymbol{\omega} = 0$), the vorticity field is also periodically reprojected onto a divergence-free space by solving a Poisson equation (additional details can be found in Ref. 14).

The Vortex Particle-Mesh method exploits the non-dispersive properties of Lagrangian methods, enabling a very accurate capture of turbulent wakes over extreme distances. It also permits using larger time steps by waiving partially the classical CFL condition associated to Eulerian methods.

The flow is not fully resolved around the rotor blades, i.e., the fine-scale boundary layers phenomena are not captured. The coarse-scale aerodynamics are rather modeled through an Immersed Lifting Line (ILL) method (Refs. 15,16), which discretizes the blades in finite segments where aerodynamic forces are obtained from airfoils polars. More specifically, a third generation Leishman-Beddoes Dynamics Stall model (Ref. 17) uses the instantaneous flow velocity and blade angle of attack to compute the lift and drag exerted on each local 2D airfoil. Then, the circulation around the airfoil is recovered from

$$\boldsymbol{l} = \rho \, \boldsymbol{V}_{\text{rel}} \times \boldsymbol{\Gamma} \tag{6}$$

with $\boldsymbol{L}$ the lift per unit span of the segment, $\boldsymbol{V}_{\text{rel}}$ the relative flow velocity and $\boldsymbol{\Gamma}$ the circulation. This circulation on a given blade segment is represented by an equivalent bound vorticity, which is then transferred to the VPM method through the release in the bulk flow of particles carrying the shed vorticity. The latter is deduced from the temporal and spanwise variations of the bound vorticity.

In order to better match realistic atmospheric conditions, the flow solver allows the injection of turbulence at the inflow of the numerical domain, which is pre-generated using the Mann algorithm (Refs. 18,19).

3.2. Multi-body solver and rotor configuration

The rigid-body mechanics of the rotor are captured through a weak coupling between the flow solver and the multi-body integrator `ROBOTRAN` (Ref. 20), which efficiently solves the direct dynamics of the multi-body system formed by the rotor hub and blades. In the present coupling, `ROBOTRAN` uses a separate temporal integrator to advance in time the state of the multi-body system, based on the aerodynamic forces computed in the flow solver, and on the rotor control inputs. After each iteration, the new positions of the lifting bodies are then communicated to the flow solver.

In the present work, a simple rotor model is used. It consists of a rotor shaft rotating at a prescribed angular velocity Ω, connected to four blades through hinges allowing two degrees of freedom per blade, respectively the flap β and pitch θ angles. The position and orientation of the rotor are prescribed. The blade flapping motion is the result of inertial and aerodynamic efforts exerted on the blades. The blade pitch is prescribed to cancel the rolling and pitching moments at the rotor hub, and to achieve the desired thrust target. This is done using the usual collective-cyclic decomposition:

$$\theta = \theta_0 + \theta_{1s} \sin \Psi + \theta_{1c} \cos \Psi \tag{7}$$

where θ_0 is the collective, θ_{1s} the lateral cyclic, θ_{1c} the longitudinal cyclic and Ψ the blade azimuthal angle (equal to zero when the blade is pointing downstream). In this work, the control input values θ_0, θ_{1s}, and θ_{1c} used in the production runs are obtained in preliminary trim simulations using a closed-loop PI controller. Their values are listed for the four airspeeds of interest in Table 1.

Table 1: Control angles of the trimmed rotor.

$\mathbf{U_\infty}$ [kt]	**100**	**50**	**25**	**12.5**
$\boldsymbol{\theta_0}$ [deg]	-4.01	-3.86	-2.83	-1.98
$\boldsymbol{\theta_{1s}}$ [deg]	-4.23	-2.15	-1.29	-0.74
$\boldsymbol{\theta_{1c}}$ [deg]	1.71	2.14	2.09	1.10

The mass of the helicopter is taken as 3000 kg. The main rotor diameter D is 10.2 m and its angular velocity is fixed to 395 RPM. Other parameters of the rotor configuration (blade pitch, hub diameter, blade twist, chord length) are taken from Ref. 21.

4. ROTORCRAFT WAKE CHARACTERIZATION

This section reports the characterization of the wake shed by a rotorcraft flying at four different airspeeds: 100, 50, 25 and 12.5 kt (i.e., respectively 51.44, 25.72, 12.86 and 6.43 $\mathrm{m\,s^{-1}}$), which are representative of various approach, landing, and taxiing flight configurations. The main objective of the study is the characterization and comparison of the wake signature at those flight speeds. The wake properties are also compared to those of the wake shed by an aircraft of similar mass flying at a typical approach speed of 100 kt.

A second objective is the assessment of the robustness of the simplified wake encounter severity metric for a follower aircraft encountering those wakes, which is the rolling moment coefficient (RMC) metric that was developed in Ref. 22 and much used in RECAT-EU (Ref. 1).

4.1. Numerical setup

The flow solver uses a uniform mesh resolution. For each case considered in this section, the spatial resolution is set to 96 grid points per rotor diameter (i.e., a Cartesian cell size of 10.625 cm), which is a compromise between accuracy and time-to-solution. The computational domain is a rectangular box. Its dimensions depend on the size of the support of the vorticity field, and thus on the flight speed: at high TAS, the wake is more compact than at low TAS but it must be simulated further downstream. Indeed, the evaluation of the wake properties must be performed at a similar "dimensionless age" t^* for each TAS. The dimensionless age of the wake at a given downstream position x is

$$t^* = \frac{t}{t_0} = \frac{x}{U_\infty\, t_0} \tag{8}$$

where

$$t_0 = \frac{b_0}{V_0} \quad \text{and} \quad V_0 = \frac{\Gamma_0}{2\pi\, b_0} \tag{9}$$

with b_0 the distance between the centers of the two rolled-up wake vortices and $\pm\Gamma_0$ the total circulation of each vortex (one being positive, the other one being negative). Therefore

$$t^* = \frac{\Gamma_0\, x}{U_\infty\, 2\pi\, b_0^2} = \frac{L\, x}{\rho\, U_\infty^2\, 2\pi\, b_0^3}\,. \tag{10}$$

At constant lift $L = \rho\, U_\infty\, \Gamma_0\, b_0$, and if b_0 remains essentially constant, then Γ_0 is inversely proportional to the TAS; thus the distance downstream where the wake has the same dimensionless age is proportional to the TAS squared: when the TAS is halved, the distance where the wake properties should be evaluated is divided by four. While the above argument will not be strictly valid for rotorcraft at low airspeeds (as the lift equation used above will then be only approximate and as b_0 will vary: see later), it nevertheless provides a proper approximate scaling.

In all cases, the computational domain extends $4D$ upstream of the rotor center. The dimensions of the computational domain for the 4 considered TAS are summarized in Table 2. The x axis is aligned with the free stream velocity (the positive direction pointing downstream) and the z axis is pointing up. The approximate total number of grid points for each simulation is 113×10^6, 71×10^6, 170×10^6 and 382×10^6, respectively at 100, 50, 25, and 12.5 kt.

Table 2: Dimensions of the computational domain.

$\mathbf{U}_\infty$ [kt]	**100**	**50**	**25**	**12.5**
$\boldsymbol{L_x/D}$ [−]	32	20	12	12
$\boldsymbol{L_y/D}$ [−]	2	2	4	6
$\boldsymbol{L_z/D}$ [−]	2	2	4	6

For each case, the simulation is first run for one convective time $t_c = L_x/U_\infty$ to ensure the full development of the wake. At 100, 50 and 25 kt, the wake statistics are computed over another two convective times. At 12.5 kt, the statistics are computed over one additional convective time.

Turbulence is injected at the inflow to simulate a weakly turbulent atmosphere, with an eddy dissipation rate of $\epsilon = 1.59 \times 10^{-5}$ m^2 s^{-3}.

4.2. Qualitative wake characteristics

Figures 1 and 2 show 3D volume renderings of the instantaneous vorticity magnitude, $\|\boldsymbol{\omega}\|$, for the wake produced by a rotorcraft flying at 100 kt, 50 kt, 25 kt and 12.5 kt.

At high and moderate airspeed (100 and 50 kt), the wake rolls up in a pair of counter-rotating vortices, which are clearly visible in Figure 1. The wake is very similar to that of a fixed-wing aircraft, with well distinguishable vortices. At low airspeed (25 kt), the wake rolls up to form a coherent two-vortex system, that is still visible in Figure 2 despite the greater complexity of the wake compared to the cases at higher TAS. At the very low speed of 12.5 kt, the wake resembles more a deformed turbulent jet. The wake vortices, although still measurable when investigating the time-averaged flow, are no longer visible in an instantaneous flow field: they are overwhelmed by the complex turbulent structures.

In the following investigations, the reported statistics and wake properties are measured in planes normal to the free stream velocity. In Eq. (10), it is shown that the distance downstream (evaluated in the x direction, and relatively to the rotor center) where the wake properties must be evaluated is essentially proportional to the TAS squared. The wake properties are measured at a distance of $24D$ at 100 kt and $6D$ at 50 kt. At 25 kt, the distance should be $1.5D$, and at 12.5 kt, it should be $0.375D$, following the approximate scaling of Eq. (10). However, as shown in Figures 3 and 4 (representing the circulation distribution, $\Gamma(r)$, around the center of the wake vortices, taken as the mean of the distributions around the port and starboard vortices), the wake cannot properly roll up on such short distances. To have a rolled-up wake (i.e., one without an overshoot in $\Gamma(r)$), the evaluation distance is set to $x = 3D$ at 25 kt, and to $x = 1.5D$ at 12.5 kt.

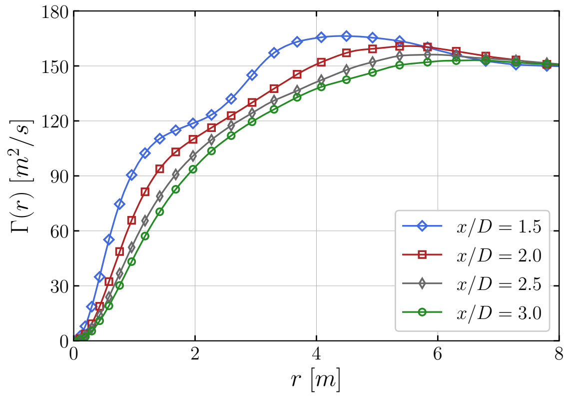

Figure 3: Wake rollup at $U_\infty = 25\ kt$: distribution of circulation $\Gamma(r)$ at various downstream locations.

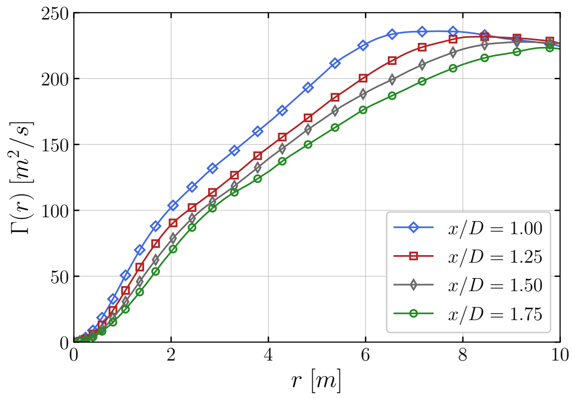

Figure 4: Wake rollup at $U_\infty = 12.5\ kt$: distribution of circulation $\Gamma(r)$ at various downstream locations.

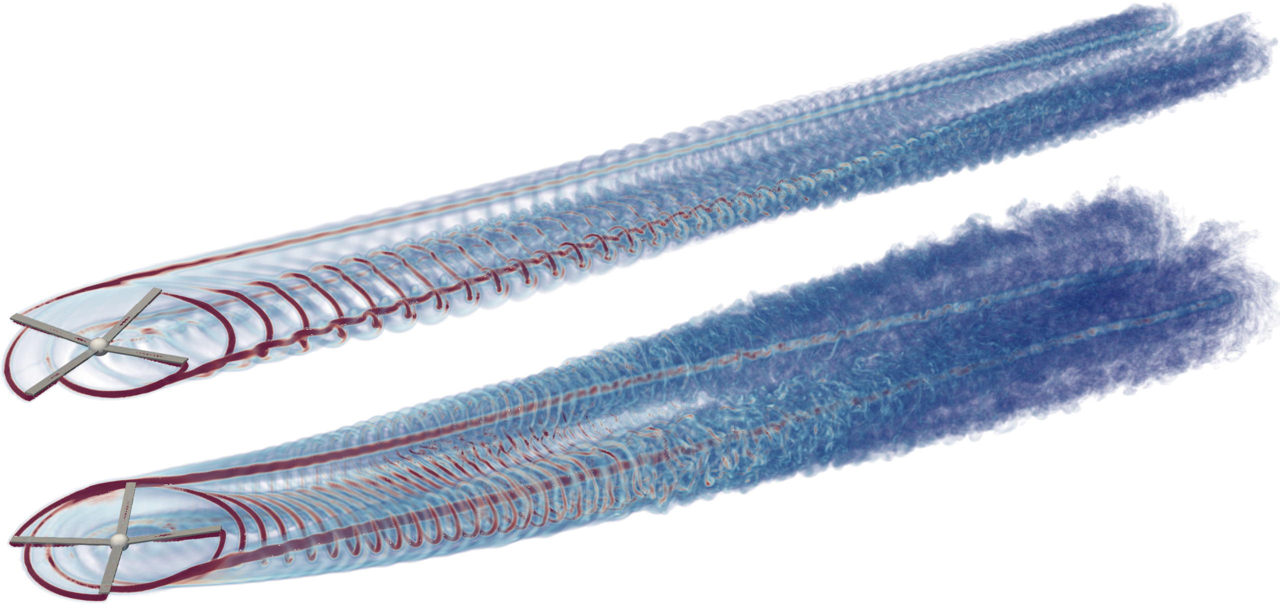

(a) Perspective view, U_∞ = 100 kt (top) and 50 kt (bottom).

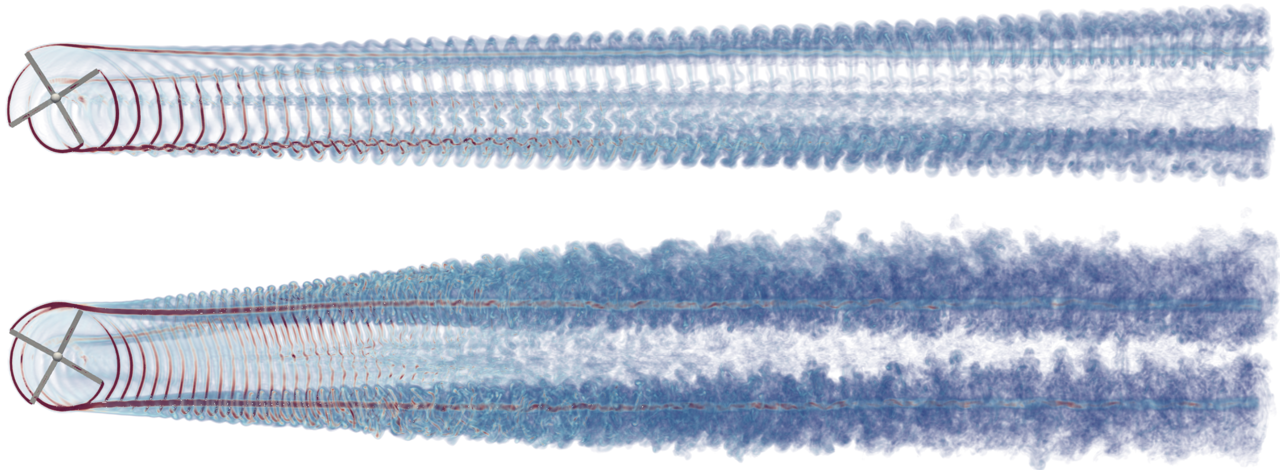

(b) Top view, U_∞ = 100 kt (top) and 50 kt (bottom).

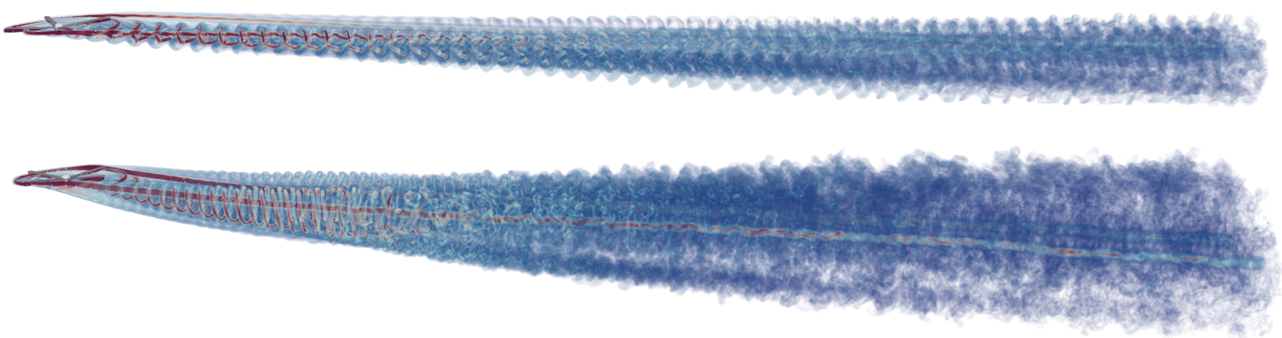

(c) Lateral view, U_∞ = 100 kt (top) and 50 kt (bottom).

Figure 1: Volume rendering of $\|\boldsymbol{\omega}\|$ showing the wake shed at 100 and 50 kt. The value of $\|\boldsymbol{\omega}\|$ is saturated between 5 and 120 s^{-1}.

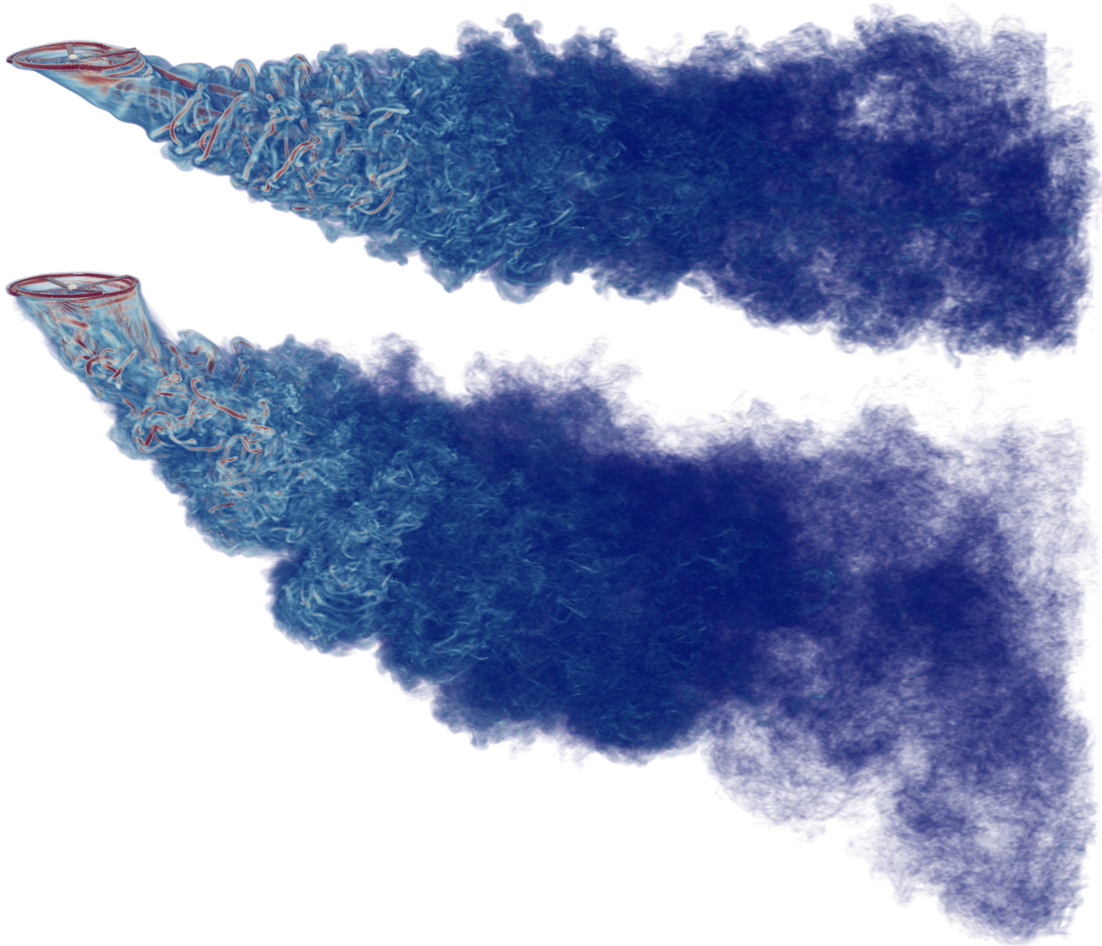

(a) Lateral view, U_∞ = 25 kt (top) and 12.5 kt (bottom).

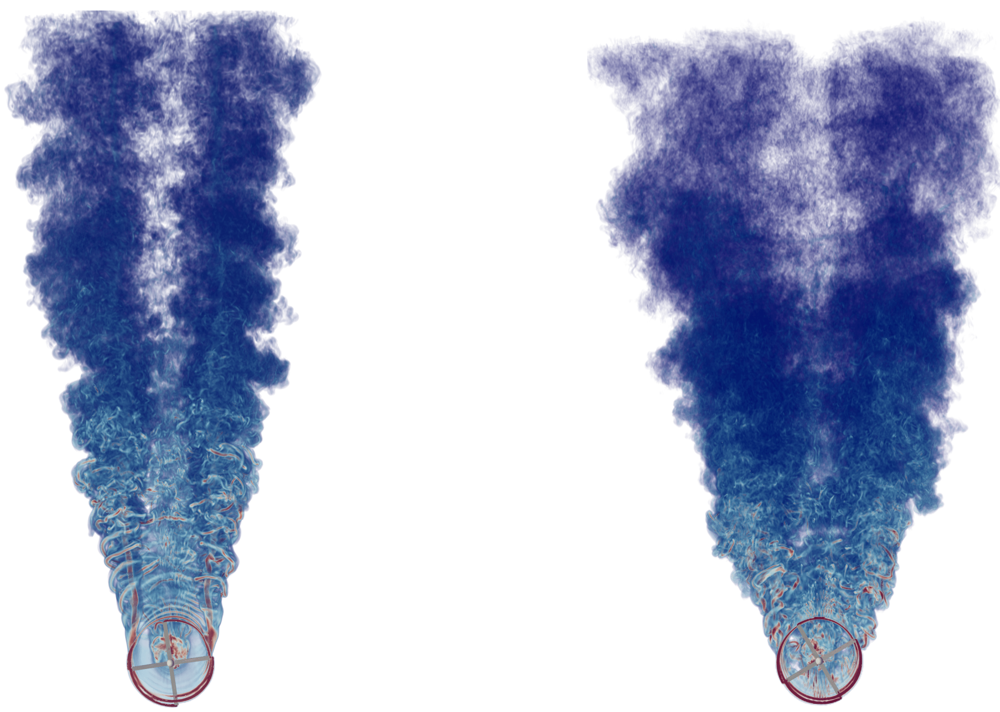

(b) Top view, U_∞ = 25 kt (left) and 12.5 kt (right).

Figure 2: Volume rendering of $\|\omega\|$ showing the wake shed at 25 and 12.5 kt. The value of $\|\omega\|$ is saturated between 5 and 170 s^{-1}.

When assessing the wake signature, it is useful to compute the time-averaged field of axial vorticity at a given downstream location x, $\overline{\omega_x}(x)$, from which one can retrieve meaningful mean wake characteristics such as the position of the vortices, their circulation distribution and induced velocity, and the core radius. Figures 5, 6, 7 and 8 show the normalized mean axial vorticity field $\frac{\overline{\omega}_x D}{U_\infty}$ at 100, 50, 25, and 12.5 kt, respectively.

At 100 kt and 50 kt, the vortex cores are clearly visible in the time-averaged field, up to far downstream. The wake is port-starboard symmetric. At 25 kt, the vortex cores are more spread out and port-starboard asymmetric. At 12.5 kt, the two-vortex system appears (as a reminder, it is not visible in the instantaneous fields) but it is much more spread out and it rapidly diffuses downstream.

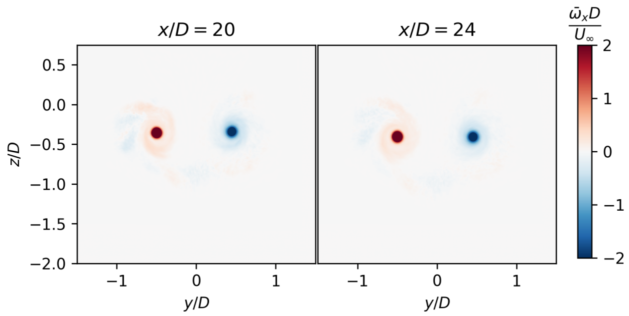

Figure 5: Normalized mean axial vorticity at 100 kt.

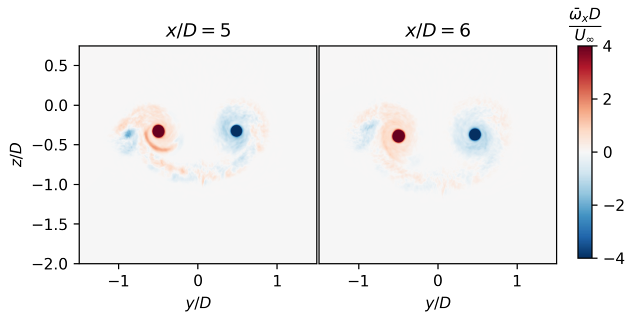

Figure 6: Normalized mean axial vorticity at 50 kt.

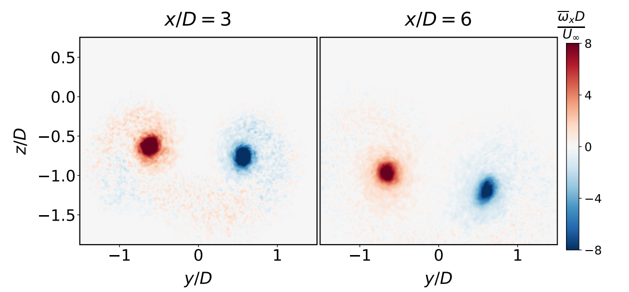

Figure 7: Normalized mean axial vorticity at 25 kt.

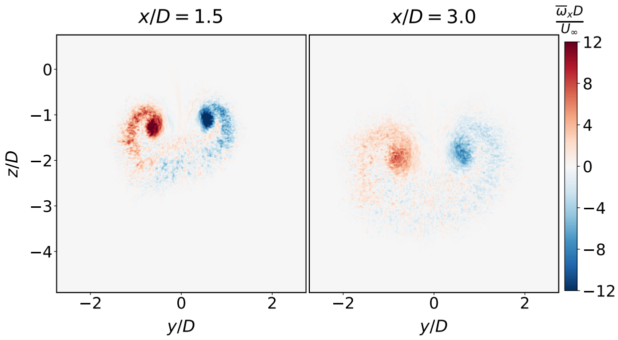

Figure 8: Normalized mean axial vorticity at 12.5 kt.

4.3. Quantitative wake characterization

A quantitative comparison of the wake properties at the four airspeeds of interest is shown in Table 3. They are also compared to those of a fixed-wing aircraft flying at 100 kt. The aircraft is based on public data of the Daher-Socata TBM 900 (with a flap setting typical of a landing configuration, Ref. 23), which has a span and mass similar to those of the rotorcraft (span $b = 12$ m and mass of 3000 kg), and is simulated using the same numerical setup as the one used for the simulation of the rotorcraft flying at 100 kt. The following quantities are measured:

- $\tilde{\Gamma}_0 = \int_{\text{half-plane}} \overline{\omega}_x \, dS$,
- $\tilde{b}_0 = \frac{I}{\tilde{\Gamma}_0}$ where $I = \int y\,\overline{\omega}_x \, dS$,
- Γ_0, the maximum value of the measured circulation distribution $\Gamma(r)$ of the wake vortices,
- b_0, the measured distance between the two wake vortex cores (the position of which is determined by optimizing the center position of a 2-D Gaussian kernel relatively to the vorticity field),
- r_c, the effective core radius (defined as the radius of maximum vortex induced velocity).

Table 3: Measured wake properties.

Type		AC	RC	RC	RC	RC
$\mathbf{U_\infty}$	[kt]	**100**	**100**	**50**	**25**	**12.5**
$\boldsymbol{x}$	[m]	$24b$	$24D$	$6D$	$3D$	$1.5D$
$\boldsymbol{\Gamma_0}$	[m^2 s^{-1}]	52.3	52.2	101	153	228
$\boldsymbol{b_0}$	[m]	8.89	9.74	9.87	12.20	12.52
$\boldsymbol{r_c}$	[m]	0.63	0.69	0.66	1.41	2.19
$\boldsymbol{\tilde{\Gamma}_0}$	[m^2 s^{-1}]	52.5	50.5	97.1	148	223
$\boldsymbol{\tilde{b}_0}$	[m]	9.09	9.30	9.72	12.63	16.05

When it is fully rolled-up, the wake shed by a wing consists of a pair of counter-rotating vortices of total circulation $\pm\Gamma_0$ and spacing b_0 between the vortex centers. The lift can then simply be expressed as a function of the flight speed and vortex properties:

$$L = \rho\, U_\infty\, \Gamma_0\, b_0 \ . \tag{11}$$

In general, the lift produced by a lifting body, such as a wing or rotor, can be expressed as (Ref. 24)

$$L = \rho \left(U_\infty \int_S y\, \overline{\omega}_x \; dS - \int_S \left(\overline{u}_x - U_\infty\right)\, \overline{u}_z \; dS \right) \tag{12}$$

where S is a plane normal to the free stream velocity and enclosing the support of ω_x.
If the axial velocity difference $\overline{u}_x - U_\infty$ (induced by the wake and also due to the parasitic drag) is negligible, Eq. (12) reduces to

$$L = \rho\, U_\infty \int_S y \overline{\omega}_x \; dS = \rho\, U_\infty\, \tilde{\Gamma}_0\, \tilde{b}_0 \ . \tag{13}$$

When the wake consists of almost axisymmetric and compact vortices with a total circulation Γ_0 easily measurable, this equation reduces to Eq. (11).

At high (100 kt) and moderate (50 kt) airspeeds, the wake of the rotorcraft rolls up in a pair of compact counter-rotating vortices, very similar to those shed by an aircraft. As seen in Table 3, the wake properties are indeed very similar between the aircraft and the rotorcraft flying at 100 kt, except for the vortex spacing which is slightly larger for the latter. At these TAS, b_0 does not vary significantly with U_∞, and Γ_0 represents a good estimation of the total half-plane circulation. The general lift equation (12) is then well-approximated by equation (11). In those cases with b_0 essentially constant, the circulation Γ_0 is essentially inversely proportional to the TAS:

$$\Gamma_0 \propto \frac{1}{U_\infty}. \tag{14}$$

At low TAS (25 kt), the two-vortex system is more diffused, with a notable increase of the core radius, but it is still relatively compact and axisymmetric. The vortex circulation is then still easily measurable. A notable observation is the significant increase in the vortex spacing b_0, which is now even larger than the rotor diameter D (the ratio being approximately 1.2). This comes as a somewhat surprising result. Indeed, for an aircraft, the vortex spacing is always smaller than the wingspan b (i.e., $b_0/b < 1$). This is thus not always the case for a rotorcraft; it is true at high and moderate airspeed, but not at low airspeed. Since the ratio b_0/D at 25 kt is not the same as that observed at 50 and 100 kt, a consequence of equation (11) is that Γ_0 is no longer inversely proportional to U_∞; it is not doubled when U_∞ is halved.

At very low TAS (12.5 kt), the mean wake departs significantly from a simple two-vortex system: the mean axial vorticity field is no longer axisymmetric around the vortex center, and its support is much less compact, see Figure 8. While equation (13) still holds, the vortex center is not well defined; even when measured approximately, it does not match with the centroid of the half-plane vorticity field (i.e., the measured b_0 differs significantly from $\tilde{b}_0$). The vorticity field being no longer axisymmetric around the measured vortex center, the concept of a circulation distribution that depends solely on the distance r to the center is also not well defined, hence measuring a value for Γ_0 is also less obvious.

It must be stressed that, for all cases, it is equation (13) which is true. When a two-vortex system is well-defined (i.e., with a well-defined center, and an essentially axisymmetric vorticity field around that center), the measured b_0 value is close to $\tilde{b}_0$ and the measured Γ_0 value is close to $\tilde{\Gamma}_0$; hence equation (11) is also valid.

4.4. Distribution of circulation and induced velocity

Figure 9 shows the radial distribution of dimensionless circulation $\Gamma(r)/\Gamma^*$ (where Γ^* is the circulation evaluated at $r = 0.7\, b_0$), for all the cases studied, and also for the aircraft flying at 100 kt.

The aircraft and the rotorcraft at 100 kt have similar circulation distributions, though the aircraft presents a monotonous increase of $\Gamma(r)$ whereas the rotorcraft shows a slight overshoot, indicative that the wake is not fully rolled-up. It could require another $10 - 15D$ to achieve a monotonous circulation distribution.

The distribution at 50 kt is very close to that at 100 kt for $r/b_0 \geq 0.2$, with the same overshoot and thus also indicative that the wake is not fully rolled-up. Interestingly, it is close to that of the aircraft at 100 kt for $r/b_0 \leq 0.2$.

At 25 kt, the shape of the circulation distribution still resembles that obtained at higher TAS; yet with a twice fatter effective core. This is no longer the case at 12.5 kt, where the shape of the distribution is very different.

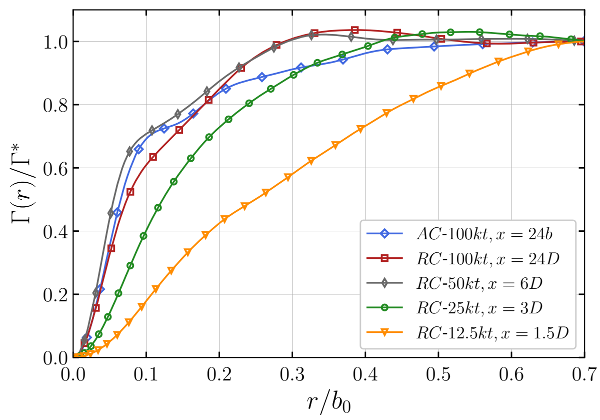

Figure 9: Distribution of the dimensionless circulation.

The radial distribution of the dimensionless induced velocity $u_\theta(r)/V_0 = (\Gamma(r)/(2\pi\, r)/V_0)$ is shown in Figure 10. The profiles are somewhat similar for the aircraft and for the rotorcraft at 100 and 50 kt, due to their similar $r_c/b_0 \simeq 0.07$. At 25 kt, $r_c/b_0 \simeq 0.12$, and hence the maximum dimensionless induced velocity is significantly lower. At 12.5 kt, $r_c/b_0 \simeq 0.18$, and hence the maximum dimensionless induced velocity is even lower.

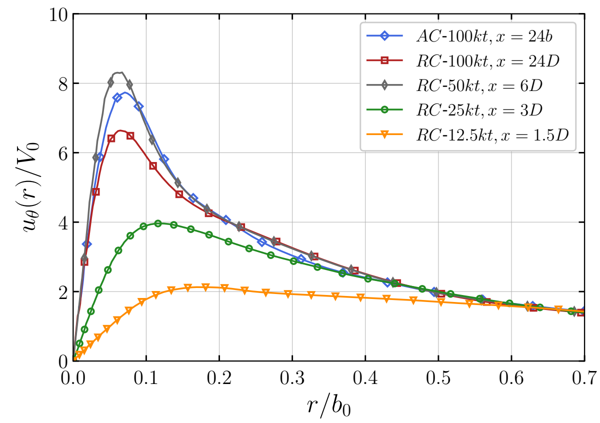

Figure 10: Distribution of the dimensionless induced velocity.

4.5. RMC metric

The simplified wake severity metric used in RECAT-EU (Ref. 1) estimates the normalized rolling moment produced on a follower aircraft when assuming an encounter centered on one wake vortex; the other one being ignored. The rolling moment coefficient (RMC) is estimated using:

$$RMC = \frac{M_{Roll}}{\frac{1}{2}\rho U_{\infty,f}^2\, S\, b} \simeq \frac{AR}{(AR+4)} \int_0^1 \frac{c(\eta)}{\bar{c}} \frac{\Gamma(\eta)}{U_{\infty,f}\, b}\, d\eta \tag{15}$$

where

- $U_{\infty,f}$ is the TAS of the follower aircraft,
- b is the span of the wing,
- S is the area of the wing,
- $\bar{c} = S/b$ is the mean chord of the wing,
- $AR = b/\bar{c}$ is the Aspect Ratio of the wing,
- $\eta = y/(b/2)$,
- $c(\eta)$ is the chord distribution of the wing.

The RMC metric computation is thus based on the measured circulation distribution around the wake vortex.

In this study, the follower aircraft is the same as the leader aircraft used for the comparison of the wake properties, i.e., the Daher-Socata TBM 900 with $U_{\infty,f} = 100\ kt$.

The values of RMC obtained for an encounter with the various wakes at a distance x_{enc} from the rotor/wing center are reported in Table 4.

Table 4: RMC values for a follower fixed-wing aircraft with $U_{\infty,f} = 100\ kt$.

Generator	**AC**	**RC**	**RC**	**RC**	**RC**
U$_\infty$ [kt]	**100**	**100**	**50**	**25**	**12.5**
x_{enc} [m]	$24b$	$24D$	$6D$	$3D$	$1.5D$
RMC [−]	0.046	0.045	0.089	0.107	0.104

The RMC obtained for a centered encounter with one vortex of the wake produced by the aircraft and rotorcraft flying at 100 kt are very close. Again, this is the consequence of their similar induced velocity profile. For the wake of the rotorcraft flying at 50 kt, as r_c/b_0 is similar to that at 100 kt and as the generator TAS is halved, the RMC is doubled. For the wake of the rotorcraft flying at 25 kt, the RMC only increases by approximately 20 %. At 12.5 kt, the RMC does not further increase.

It should be noted that, at low TAS and very low TAS, the RMC metric strongly depends on the streamwise position where it is measured, as illustrated in Figure 11. This is due to the fast "aging process" of those wake vortices, which is indeed significant when the wake is very turbulent, so that the effective core radius increases fast. Through this mechanism, the vortices interact significantly with each other through the mid-plane, making the circulation of each vortex decrease. For the wake produced at 25 kt, the RMC value is seen to decrease by 15 % between $x = 3D$ and $x = 6D$. For the wake produced at 12.5 kt, the RMC value decreases by 48 % between $x = 1.5D$ and $x = 6D$.

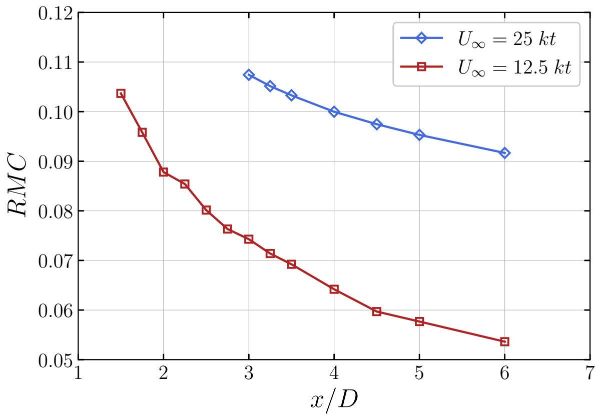

Figure 11: Variation of the RMC with the normalized streamwise distance x/D for the wakes of rotorcraft at low TAS and very low TAS.

5. ROTORCRAFT ENCOUNTERING A WAKE

This section summarizes the results regarding the wake encounter by a rotorcraft, aiming to quantify the upset on a follower rotorcraft resulting from its interaction with the wake of a leader aircraft or rotorcraft. This is done by measuring the wake-induced forces and moments undergone by the rotor when crossing the wake vortices on an oblique trajectory at a small angle and at the altitude of their centers.

Three airspeeds of the follower rotorcraft are investigated: 100, 50 and 25 kt. In these simulations, the encountered wake is that produced by the same rotorcraft flying at 100 kt.

5.1. Numerical setup

The numerical solver, the rotor configuration and its trim are identical to those presented in Sections 3 and 4. The wake of the leader rotorcraft flying at 100 kt is represented by a pair of rolled-up vortices obtained from the wake characterization (cf. Section 4), which are continuously fed into the computational domain.

The wake encounter is simulated on an imposed trajectory since the aim is to measure the forces and moments felt by the follower, not its dynamic response. The follower rotorcraft is initially located at a lateral distance of $4D$ relative to the center of the two-vortex system. In an initial phase, it flies parallel to the wake vortices, so as to properly establish its own wake. When the latter is well developed, the rotorcraft changes direction to achieve an oblique trajectory with a lateral speed component of 5 kt with respect to the two-vortex system. It was verified that, as long as it remained small compared to the TAS, the magnitude of that lateral component had little impact on the forces and moments felt by the rotor, which are thus very close to those that would be measured at any position along the trajectory if the rotor was maintained fixed at that position.

While accelerating laterally to reach the aimed lateral speed value, the rotor also aligns itself with the new oblique velocity vector, the magnitude of which is the TAS and is kept constant. Thus, the trim remains valid as the TAS is maintained. Once the terminal lateral speed is reached, the helicopter maintains its velocity until the end of the simulation. The trim is also maintained; hence the forces and moments that are measured when crossing the wake are solely due to the influence of that wake on the rotor.

The spatial resolution is 64 points per rotor diameter. Through a convergence study (not shown here), this resolution was demonstrated as sufficient to capture the wake encounter phenomena. The computational domain extends $2D$ upstream of the rotor center. At 100 kt, it extends $10D$ downstream; at 50 and 25 kt, it extends $6D$ downstream. The lateral and vertical dimensions of the computational domain dynamically adapt to the positions of the rotorcraft and of its wake. No atmospheric turbulence is added for the wake crossing simulations.

5.2. Wake-induced aerodynamic loads

Volume renderings of the vorticity magnitude illustrating the rotorcraft after the wake crossing are shown in Figures 12 and 13, respectively at 50 and 25 kt.

Figure 14 shows the wake-induced perturbations in yawing, pitching and rolling moments, as well as in lift force, as a function of the lateral distance of the rotor with respect to the vortices. This corresponds to a port encounter, i.e., a wake encounter where the port side of the rotor first reaches the starboard wake vortex.

The principal wake-induced loads are a yawing moment, a pitching moment, and a lift force. The yaw and lift perturbations as a function of the lateral position of the rotorcraft are essentially symmetric with respect to the center of the wake, whereas the pitching moment is essentially anti-symmetric.

Figure 12: Volume rendering of $\|\boldsymbol{\omega}\|$ for the case of wake crossing at 50 kt. The value of $\|\boldsymbol{\omega}\|$ is saturated between 0 and 110 s^{-1}.

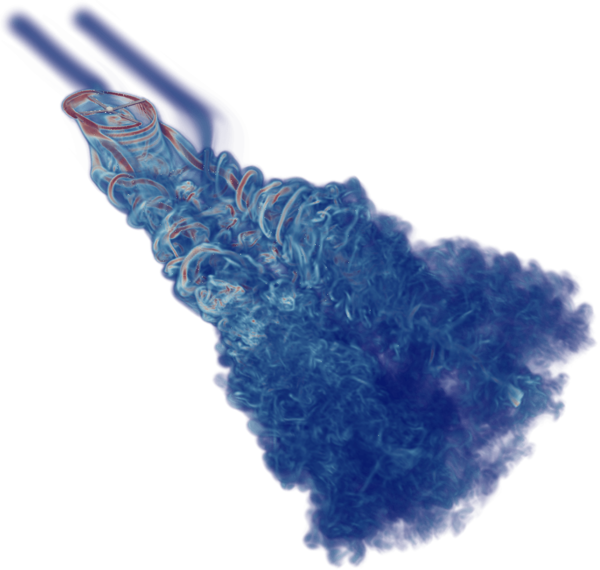

Figure 13: Volume rendering of $\|\boldsymbol{\omega}\|$ for the case of wake crossing at 25 kt. The value of $\|\boldsymbol{\omega}\|$ is saturated between 0 and 110 s^{-1}.

While a fixed-wing aircraft is mostly affected in rolling moment and lift when crossing a pair of counter-rotating vortices, the effect on a rotorcraft is a pitching moment (nose-down for a port encounter, nose-up for a starboard encounter). This corresponds to the fundamental 90° phase shift of flapping rotors (See Ref. 25).

The pitching moment M_{Pitch} has a similar profile at 100 and 50 kt, with extreme values reached when in the center of the vortices. At 25 kt, the pitching moment is less smooth: at this low airspeed, the rotorcraft is indeed more sensitive to variations in its own wake.

Interestingly, the numerical results reveal a monotonic relationship between the maximum value of M_{Pitch} and the flight speed U_∞. This is a rather counter-intuitive observation as the wake-induced velocity field is not related to the flight speed. The resulting velocity field as felt by the blades is thus not a simple superposition of the wake-induced and rotor-induced velocity fields. This constitutes a strong indicator of non-linear coupling between the wake-induced velocity field and the blade aerodynamics, resulting from the combination of several phenomena: the azimuthal asymmetry of the disk loading (between the advancing and retreating sides of the rotor); the wake-induced alteration of the blade angle of attack; and the blade flapping, a feature suspected to play a major role in this non-linear effect.

5.3. Equivalent lateral cyclic angle

As proposed in Ref. 26, the pitching moment due to the velocity field induced by the wake vortex is equivalent to that due to a certain value of the lateral cyclic angle θ_{1s}. This equivalent lateral cyclic angle can thus be used as a metric to characterize the wake encounter.

The largest pitching moment experienced by a rotorcraft flying in a wake corresponds to flying in the center of the vortex. The velocity $v_{vort}(r)$ induced by the vortex produces a variation of angle of attack $\alpha_{vort}(r) = v_{vort}(r)/(\Omega\, r)$ on the blades, resulting in a modification of the blades loading, and consequently in a pitching moment. In order to characterize the effect of the wake on the rotorcraft dynamics, a theoretical equivalent lateral cyclic pitch angle $\theta_{1s,eq}$ (corresponding to a velocity $v_{cyc}(r) = (\Omega\, r)\, \theta_{1s,eq}$) is defined. It corresponds to the virtual cyclic control input required to produce a pitching moment equivalent to that induced by a vortex-centered encounter.

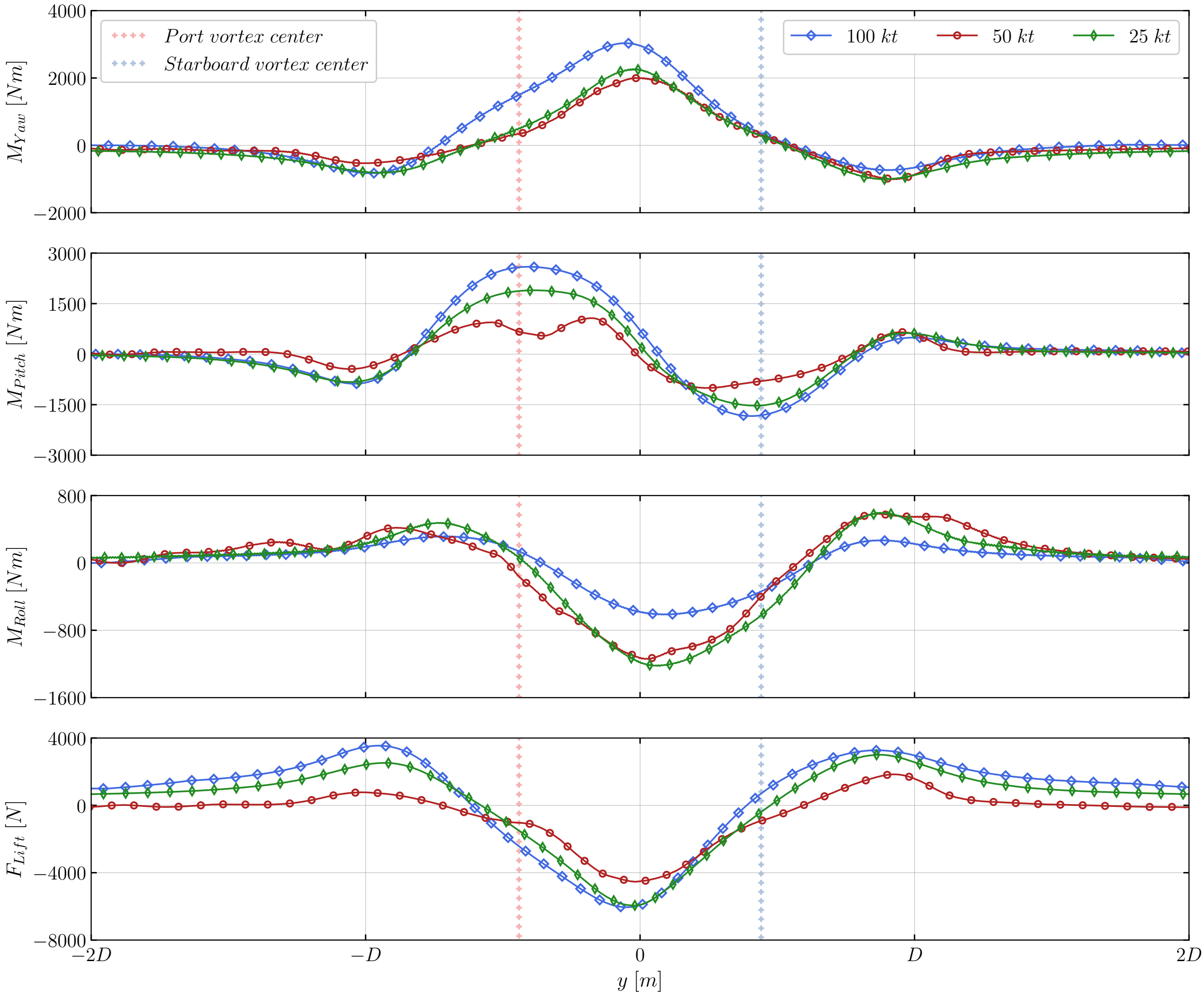

Figure 14: Aerodynamic moments and lift upsets resulting from the wake encounter at 100, 50 and 25 kt.

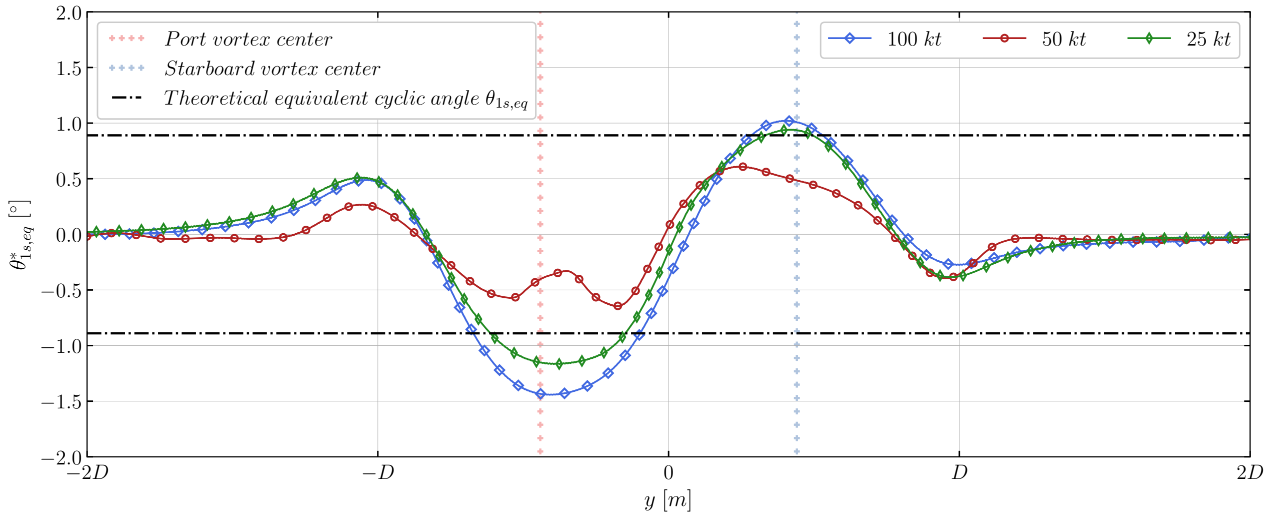

Figure 15: Computed equivalent lateral cyclic angle as a function of the rotorcraft lateral position at 100, 50 and 25 kt.

It is obtained by equating the moment induced by the wake with the moment induced by the virtual lateral cyclic angle (see Ref. 25):

$$\begin{aligned} & \int_0^R \frac{1}{2}\rho\,(\Omega\,r)^2\,c(r)\,C_{l,\alpha}\,\alpha_{vort}(r)\,r\,dr \\ = & \int_0^R \frac{1}{2}\rho\,(\Omega\,r)^2\,c(r)\,C_{l,\alpha}\,\theta_{1s,eq}\,r\,dr \end{aligned} \tag{16}$$

where $C_{l,\alpha}$ is the aerodynamic derivative of the local airfoil and R is the rotor radius. Further assuming that the blade chord c does not vary with r, this simplifies to:

$$\int_0^R v_{vort}(r)\,r^2\,dr = \int_0^R \left((\Omega\,r)\,\theta_{1s,eq}\right)\,r^2\,dr \tag{17}$$

Thus

$$\theta_{1s,eq} = \frac{4}{\Omega\,R^4}\int_0^R v_{vort}(r)\,r^2\,dr \tag{18}$$

For an encounter with the wake shed by a leader rotorcraft flying at 100 kt, and using its measured circulation distribution, this gives $\theta_{1s,eq} = 0.89°$.

It must be emphasized that the above very simplified analysis was made without taking into account the forward velocity of the follower rotorcraft; thus in hover. It can only be hoped to be also applicable for a rotorcraft in forward flight.

To test the validity of the above simplified theoretical formula in forward flight, one can compute the true equivalent cyclic control angle based on the measured pitching moment, $\theta^*_{1s,eq}$. This is achieved by computing the derivative of the pitching moment with respect to the lateral cyclic angle, $M_{Pitch,\theta_{1s}} = \frac{\partial M_{Pitch}}{\partial \theta_{1s}}$. This derivative is obtained by measuring M_{Pitch} for several values of θ_{1s} in steady conditions, and then by performing a linear regression on the obtained data. The measured derivative is reported in Table 5 for the three TAS of interest.

Table 5: Pitch control derivative.

U$_\infty$	[kt]	**100**	**50**	**25**
$\boldsymbol{M_{pitch,\theta_{1s}}}$	[Nm/deg]	- 1800	- 413	- 102

The equivalent lateral cycling angle is then computed as follows:

$$\theta^*_{1s,eq} = \frac{M_{Pitch}}{M_{Pitch,\theta_{1s}}} \tag{19}$$

The result is presented in Figure 15 for the three TAS of interest, and also compared to the theoretical equivalent cyclic angle $\theta_{1s,eq}$ which does not take into account the flight speed.

The maximum and minimum values of the equivalent lateral cyclic angle for the three TAS of interest are reported in Table 6.

Table 6: Extrema of the computed equivalent lateral cyclic angle.

U$_\infty$	[kt]	**100**	**50**	**25**
max ($\boldsymbol{\theta^*_{1s,eq}}$)	[deg]	- 1.40	- 1.12	- 0.55
min ($\boldsymbol{\theta^*_{1s,eq}}$)	[deg]	1.13	0.85	0.57

The simplified metric predicts an equivalent angle of $0.89°$ regardless of the follower airspeed. At 100 and 50 kt, the simplified metric underestimates the actual maximum equivalent angle; at 25 kt, it overestimates it. While the order of magnitude provided by the simplified metric and the actual measured values are similar, the differences are significant. However, due to the port-starboard anti-symmetry of the local relative velocity seen by the blades in advancing flight and the simplified linear character of Eq. (16), it is not possible to take U_∞ into account in such a simplified approach.

6. CONCLUSIONS

A numerical solver using the Vortex Particle-Mesh method for the Large Eddy Simulation of aerodynamic wakes using Immersed Lifting Lines, and coupled to a multi-body rigid dynamics integrator, was briefly presented. It was used to simulate the wake of a rotorcraft flying at various airspeeds, to investigate the effect of the flight speed on the wake properties, and to compare the wake of a rotorcraft with the well-known wake of a fixed-wing aircraft. Then, the solver was used to study the forces and moments felt by a rotorcraft crossing a fully rolled-up wake, and to investigate the sensitivity of the wake-induced perturbation to the flight speed of the follower rotorcraft. Several conclusions can be drawn from this work:

1. At high and moderate airspeeds (100 and 50 kt), the wake of the rotorcraft rolls up similarly to that of an aircraft. At lower airspeed, the behavior of the wake departs from that of classic rolled-up wakes. At 25 kt, the vortex cores are still visible in the mean wake, but the spacing b_0 between the vortices is significantly larger. At 12.5 kt, the wake

resembles more a deformed turbulent jet; despite being visible in the mean vorticity field, the two-vortex system is much more spread out and no longer axisymmetric.

2. At high and moderate airspeeds (100 and 50 kt), the simplified lift equation, $L = \rho U_\infty \Gamma_0 b_0$, holds with good accuracy. Since the obtained vortex spacing is approximately equal at both speeds, the total circulation is essentially inversely proportional to the flight speed. At low and very low speeds (25 and 12.5 kt), the vortex circulation Γ_0 is no longer doubled when the TAS is halved, due to the significant increase in the vortex spacing b_0; and also to the difficulty of defining a vortex center at 12.5 kt.

3. The RMC is almost identical for the wakes of aircraft and rotorcraft flying at 100 kt. At 50 kt, it is essentially doubled. However, at lower airspeed, the RMC is no longer inversely proportional to the TAS. Moreover, at low airspeed, the RMC rapidly decreases with the downstream distance, due to the strong turbulence in the wake, leading to a fast decay of the vortices.

4. The effect of a wake on a follower rotorcraft is a pitching moment (for an aircraft, the main perturbation is a rolling moment). A proportionality relationship between the maximum pitching moment and the airspeed of the follower was observed, suggesting significant non-linearities in the interaction between the wake and the rotor blades.

5. The simplified metric of Ref. 26 for the pitch perturbation in the form of an equivalent lateral cyclic angle was assessed. However, since it does not take into account the airspeed of the follower rotorcraft, it fails to properly capture the proportionality relationship that was observed between the maximum pitching perturbation and the airspeed of the follower.

Author contact:

Guillaume Querinjean
guillaume.querinjean@uclouvain.be

7. ACKNOWLEDGMENTS

Financial support and scientific input from Eurocontrol, through three research contracts, are gratefully acknowledged. G. Querinjean is a FRIA grantee of the Fonds de la Recherche Scientifique (F.R.S-FNRS). Computational resources have been provided by the supercomputing facilities of UCLouvain (CISM) and the Consortium des Équipements de Calcul Intensif en Fédération Wallonie Bruxelles (CÉCI) funded by the F.R.S.-FNRS and by the Walloon Region. The present research benefited from computational resources made available on Lucia, the Tier-1 supercomputer of the Walloon Region, infrastructure funded by the Walloon Region under the grant agreement n°1910247.

8. REFERENCES

1. Graham, F., Rooseleer, F., Treve, V. and De Visscher, I., “Wake turbulence re-categorisation on approach and departure for safe and more efficient air traffic management “, 30th Congress of the International Council of the Aeronautical Sciences, 2016.

2. Poinsot, T., Corjon, A., “Vortex model to define safe aircraft separation distances”, *Journal of Aircraft*, Vol. 33, (3), 1996, pp. 547-553, DOI: 10.2514/3.46979.

3. Zhou, J., Chen, Y., Li, D., Zhang, Z., and Pan, W., “Numerical simulation of aircraft wake vortex evolution and wake encounters based on adaptive mesh method”, *Engineering Applications of Computational Fluid Mechanics*, Vol. 14, (1), 2020, pp. 1445-1457, DOI: 10.1080/19942060.2020.1835736.

4. Winckelmans, G., and Capart, R., “Wake vortex induced rolling moment on a follower aircraft”, AWIATOR technical note AWUCL-114-001, 2004.

5. Jimenez-Garcia, A., Barakos, G.N., Treve, V., Rooseleer, F., Cappellazzo, V., and Graham, R, “Helicopter Wake Encounters in the Context of RECAT-EU”, 43rd European Rotorcraft Forum Proceedings, Milan, September 2017.

6. Line, A.J., Brown, R.E., “Efficient high-resolution wake modeling using the vorticity transport equation”, *AIAA journal*, Vol. 43, (7), 2005, pp. 1434–1443, DOI: 10.2514/1.13679.

7. He, C. and Zhao, J., “Modeling rotor wake dynamics with viscous vortex particle method”, *AIAA journal*, Vol. 47, (4), 2009, pp. 902–915, DOI: 10.2514/1.36466.

8. Caprace, D.-G., Chatelain, P., and Winckelmans, G., “Wakes of rotorcraft in advancing flight: A large-eddy simulation study”, *Physics of Fluids*, Vol. 32, (8), 2020, DOI: 10.1063/5.0015162.

9. Caprace, D.-G., and Ning, A., “Large Eddy Simulation for Empirical Modeling of the Wake of Three Urban Air Mobility Vehicles”, *Journal of the American Helicopter Society*, Vol. 68, (4), 2023, pp. 42002-42017, DOI: 10.4050/JAHS.68.042002.

10. Wang, Y., White, M., Barakos, G.N., Tormey, P., and Pantazopoulou, P., “Simulation of a light aircraft encountering a helicopter wake”, *Journal of Aircraft*, Vol. 52, (2), 2015, pp. 510-523, DOI: 10.2514/1.C032761.

11. Chatelain, P., Curioni, A., Bergdorf, M., Rossinelli, D., Andreoni, W., and Koumoutsakos, P., “Billion vortex particle direct numerical simulations of aircraft wakes”, *Computer Methods in Applied Mechanics and Engineering*, Vol. 197, (13-16), 2008, pp. 1296–1304, DOI: 10.1016/j.cma.2007.11.016.

12. I. F. Sbalzarini, J. H. Walther, M. Bergdorf, S. E. Hieber, E. M. Kotsalis, and P. Koumoutsakos, “PPM a highly efficient parallel particle mesh library for the simulation of continuum systems,” *Journal of Computational Physics*, vol. 215, pp. 566–588, July 2006.

13. R. Cocle, G. Winckelmans, and G. Daeninck, “Combining the vortex-in-cell and parallel fast multipole methods for efficient domain decomposition simulations”, *Journal of Computational Physics*, vol. 227, pp. 9091–9120, Nov 2008.

14. G. S. Winckelmans, Encyclopedia of Computational Mechanics, ch. Vortex Methods, pp. 129–153. John Wiley and Sons, Ltd, 2004.

15. Caprace, D.-G., Chatelain, P., and Winckelmans, G., “Lifting line with various mollifications: theory and application to an elliptical wing”, *AIAA Journal*, Vol. 57, (1), 2019, pp. 17-28.

16. Caprace, D.-G., Chatelain, P., and Winckelmans, G., “An immersed lifting and dragging line model for the vortex particle-mesh method”, *Theoretical and Computational Fluid Dynamics*, Vol. 34, (1-2), 2020, pp. 21-48.

17. E. Dyachuk, A. Goude, and H. Bernhoff, “Dynamic stall modeling for the conditions of vertical axis wind turbines,” *AIAA journal*, vol. 52, no. 1, pp. 72–81, 2013.

18. J. Mann, ”Wind field simulation”, *Probabilistic engineering mechanics*, 13(4):269–282, 1998.

19. I. De Visscher, ”Interaction of wake vortices with the atmosphere and the ground: Advanced numerical simulation and operational modeling”, PhD thesis, Université catholique de Louvain (UCLouvain), 2012.

20. Docquier, N., Poncelet, A., and Fisette, P., “Robotran: a powerful symbolic generator of multibody models”, *Mechanical Sciences*, Vol. 4, (1), 2013, pp. 199–219, DOI: 10.5294/ms-4-199-2013.

21. K. Kampa, B. Enenkl, G. Polz, G. Roth, ”Aeromechanic aspects in the design of the EC135”, *Journal of the American Helicopter Society*, 44(2):83–93, 1999.

22. G. Winckelmans and I. De Visscher, ”Complement note on metrics for the rolling moment coefficient and the equivalent roll rate due to encounter of an aircraft with a wake vortex”, Technical report, UCLouvain, 2013.

23. Daher Socata, “TBM 900 pilot’s information manual”, 2017.

24. D.-G. Caprace, ”Modeling of lifting-dragging devices for large eddy simulation of space-developing wakes : application to wings, rotors and formation flight”, PhD thesis, Université catholique de Louvain (UCLouvain), 2020.

25. G.D. Padfield, ”Helicopter flight dynamics: the theory and application of flying qualities and simulation modeling”, John Wiley and Sons, 2008.

26. G. D. Padfield, B. Lawrence, and A. Taghizad, ”Rotorcraft wake vortex encounters: A flight mechanics perspective”, 32nd European Rotorcraft Forum Proceedings, Maastricht, September 2006.